Resonant evanescent excitation of guided waves with high-order optical angular momentum

Manfred Hammer, Lena Ebers, and Jens Förstner*

Theoretical Electrical Engineering, Paderborn University, Paderborn, Germany

Abstract: Gaussian-beam-like bundles of semi-guided waves propagating in a dielectric slab can excite modes with high-order optical angular momentum supported by a circular fiber. We consider a multimode step-index fiber with high-index coating, where the waves in the slab are evanescently coupled to the modes of the fiber. Conditions for effective resonant interaction are identified. Based on a hybrid analytical-numerical coupled mode model, our simulations predict that substantial fractions of the input power can be focused into waves with specific orbital angular momentum, of excellent purity, with a clear distinction between degenerate modes with opposite vorticity.

Keywords: photonics, integrated optics, dielectric resonators, modes of dielectric fibers/rods, orbital angular momentum modes, oblique excitation by semi-guided waves.

1 Introduction

Optical electromagnetic fields that carry orbital angular momentum [1–4] and thus exhibit optical vortices [5] have been studied already over some period of time. Applications are manifold, ranging from harnessing the mechanical torque [1] to optical telecommunications [4] and nonlinear and quantum optics [3]. A variety of methods for the generation of these waves have been discussed, targeting either free-space beams or specific modes in circular optical fibers. These include spiral phase plates [6], tailored lens arrangements [7], spatial light modulators [8], and helical gratings [9, 10], as well as other grating- or metasurface-based devices. Among the more sophisticated proposals are specially designed and steered fiber couplers [11], or a scheme that employs nonlinear parametric processes [12].

As a potential alternative, we have recently investigated a scheme for the resonant evanescent excitation of guided modes with orbital angular momentum (OAM) in a dielectric tube [13], considering a structure similar to Fig. 1. On the basis of a 2.5-D coupled mode model with semi-guided plane waves in the slab, we could show a possibility for the selective excitation of one of a pair of degenerate OAM modes with opposite vorticity. As a follow-up, in this paper we look quantitatively at the excitation process, for a more realistic scenario with incoming semi-guided wave bundles of laterally Gaussian shape.

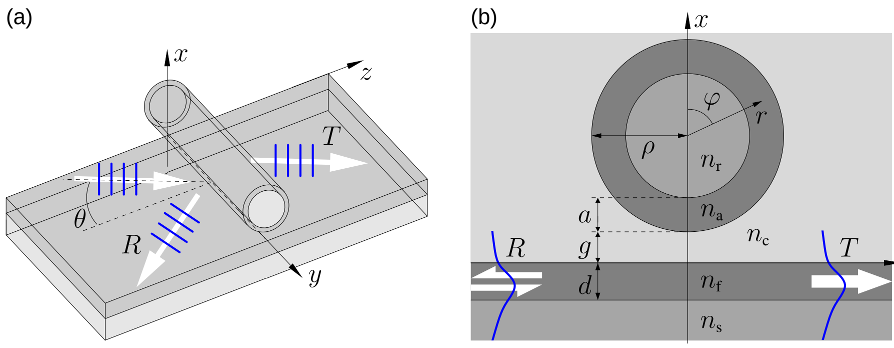

Figure 1: Evanescent excitation of a coated circular dielectric rod, schematic (a), and cross section view (b). Cartesian coordinates x, y, z are introduced, with x normal to the slab plane and y parallel to the rod axis; polar coordinates r, φ are positioned at the rod center. Incoming TE- or TM-polarized semi-guided waves propagate in the y-z-plane at an angle θ with respect to the fiber axis normal. Outgoing polarized waves with reflectance R and transmittance T are observed under potentially different angles. Parameters: refractive indices $n_s = 1.45$ (substrate), $n_f = 3.45$ (film), $n_c = 1.0$ (cladding), and $n_r = 1.45$ (rod core), $n_a = 3.45$ (rod coating); slab thickness $d = 0.22\,\mu$m, radius of the coated rod $\rho = 2\,\mu$m, coating thickness $a = 0.22\,\mu$m, variable gap g. Excitation around a vacuum wavelength $\lambda = 1.55\,\mu$m is considered.

*Paderborn University, FG Theoretical Electrical Engineering Warburger Straße 100, 33098 Paderborn, Germany
Phone: ++49(0)5251/60-3560 Fax: ++49(0)5251/60-3524 E-mail: manfred.hammer@uni-paderborn.de

In preparation for the actual 3-D simulations, Section 2 discusses some more fundamental aspects of the prior 2.5-D models [14], specifically for the configuration of Fig. 1. Section 3 summarizes our results for the fiber being excited by laterally unlimited semi-guided plane waves. In Section 4, we take bundles of these 2.5-D fields to build approximate solutions to the excitation problem for incoming semi-guided beams, in full 3-D.

The peculiarities found in the oblique excitation of infinite structures [14], with two-dimensional cross sections, form a further context of the present paper. Among the proposals that exploit these features are step- and corner-folds in slab waveguides [15–17], an anti-reflection-coating of a slab waveguide transition [18], and configurations that realize filter functions related to bound states in the continuum (BIC states) [19–22] and resonances of Fano-type [23] in a setting of waveguide photonics. Also the slab-coupled microstrip of Ref. [24] belongs to this list, with the rather remarkable filter properties of an "unlimited" Q-factor, accompanied by a strong field enhancement, that we shall also observe for the present structure.

2 Semi-guided waves

We consider the slab-coupled fiber of Fig. 1. Half-infinite slabs connect to a central domain of interest, that includes the fiber with high-index coating, and the slab region underneath. Incoming and potentially reflected waves ($z < 0$), and transmitted waves ($z > 0$), propagate in these slabs at oblique angles. Arguments from Refs. [13, 14, 16, 25] apply, that are given here for reasons of consistency, adapted to our specific configuration.

This concerns time harmonic fields $\sim \exp(\mathrm{i}\omega t)$ with angular frequency $\omega = k\mathrm{c} = 2\pi\mathrm{c}/\lambda$, for vacuum wavelength λ, wavenumber k and speed of light c. The input wave

$$\sim \mathbf{\Psi}_{\text{in}}(k_y; x)\ \mathrm{e}^{-\mathrm{i}(k_y y + k_z z)}, \qquad \text{with} \qquad k_y = kN_{\text{in}} \sin\theta, \tag{1}$$

has the form of a TE- or TM-polarized guided mode with vectorial profile $\mathbf{\Psi}_{\text{in}}(k_y; x)$ and effective mode index N_{in} (cf. Refs. [25, 26]), propagating at angle θ in the y-z-plane (cf. Fig. 1(a)), with wavenumbers k_y and k_z, where $k_z = kN_{\text{in}} \cos\theta$, and $k_y^2 + k_z^2 = k^2 N_{\text{in}}^2$. The structure is constant along the y-axis, and we look for fields that are stationary along y. The total solution can thus be restricted to the single spatial Fourier component k_y of the incident wave, where the angle of incidence θ determines the wavenumber k_y according to Eq. (1).

Next we focus on a particular outgoing wave, which can be a guided TE- or TM-mode of the slab, propagating in positive ($\zeta = z$) or negative ($\zeta = -z$) direction z, but also some non-guided wave that radiates away from the region of interest in a direction ζ in the x-z-plane. Analogously to Eq. (1), one can assume a modal form with profile $\mathbf{\Psi}_{\text{out}}$, effective index N_{out}, and functional dependence

$$\sim \mathbf{\Psi}_{\text{out}}(k_y; \xi)\ \mathrm{e}^{-\mathrm{i}(k_y y + k_\zeta \zeta)}, \quad \text{with} \quad k^2 N_{\text{out}}^2 = k_y^2 + k_\zeta^2. \tag{2}$$

Here ξ is the cross-sectional coordinate of the mode profile in the direction perpendicular to ζ; the wave equation [25] relates the cross-sectional wavenumber k_ζ to the former k_y and the propagation constant kN_{out}. Through Eq. (2), the angle of incidence θ determines the propagation character of that particular outgoing mode.

If the effective mode index N_{out} is of a magnitude $k^2 N_{\text{out}}^2 > k_y^2$ such that k_ζ is real, the outgoing field propagates with wavenumber $k_\zeta = kN_{\text{out}} \cos\theta_{\text{out}}$ at an angle θ_{out}. The angles of incidence and refraction, and the effective indices of the incoming and outgoing waves, are linked by a relation $N_{\text{out}} \sin\theta_{\text{out}} = N_{\text{in}} \sin\theta$ in the form of Snell's law. Outgoing modes with smaller effective index N_{out}, however, with $k^2 N_{\text{out}}^2 < k_y^2$, have imaginary wavenumbers $k_\zeta = -\mathrm{i}\sqrt{k_y^2 - k^2 N_{\text{out}}^2}$. These evanescent fields do not carry any optical power [27], although they can well contribute significantly to the overall field in the central region of interest. Hence, for some pair of outgoing and incoming modes with effective indices $N_{\text{out}} < N_{\text{in}}$, a critical angle θ_{cr} can be defined as

$$\sin\theta_{\text{cr}} = N_{\text{out}}/N_{\text{in}}, \tag{3}$$

such that the type of the outgoing mode changes from ζ-propagating for $\theta < \theta_{\text{cr}}$ to ζ-evanescent, if $\theta > \theta_{\text{cr}}$.

A few immediate conclusions can be drawn specifically for the device of Fig. 1: All outgoing radiative modes, with oscillatory behavior in the substrate and/or cladding regions ("substrate/cladding modes"), have effective indices below the upper limits n_{s} or n_{c} of the respective radiation continua. Their characteristic angles (3) are thus smaller than the critical angles $\sin\theta_\mathrm{s} = n_\mathrm{s}/N_\mathrm{in}$ and $\sin\theta_\mathrm{c} = n_\mathrm{c}/N_\mathrm{in}$ associated with the substrate and cladding refractive indices. Consequently, assuming $n_\mathrm{c} < n_\mathrm{s}$, radiation into the cladding region is suppressed for $\theta_\mathrm{c} < \theta < \theta_\mathrm{s}$, while radiation into the substrate is not. For incidence at angles $\theta > \theta_\mathrm{s}$, all radiation losses vanish.

Further, the effective indices of all outgoing TM waves are below the level N_TM of the fundamental TM mode of the slab. In case of TE excitation, their characteristic angles (3) are thus smaller than the critical angle $\sin\theta_\mathrm{TM} = N_\mathrm{TM}/N_\mathrm{TE}$ associated with the fundamental TM wave. Hence, for TE incidence at angles $\theta > \theta_\mathrm{TM}$, all incident optical power is carried away by outgoing guided TE modes.

3 Evanescent excitation of a coated dielectric rod

A composite structure as in Fig. 1 is typically discussed in terms of interactions between the eigenstates of its constituents [28–30]. We apply a specific, hybrid-analytical / numerical variant (HCMT) of coupled mode theory [31]. The model requires a physically plausible ansatz, a "template", for the (approximate) optical electromagnetic field, here consisting of separate contributions related to the slab waveguide, and to the fiber. In case of the slab, one writes vectorial expressions similar to Eqs. (1), (2) for the fundamental TE- and TM-modes, for propagation in positive and negative z-direction, that implement oblique propagation at the global wavenumber k_y. Terms for the individual polarized directional modes are superimposed with amplitudes that are functions of the propagation coordinate z. The amplitude functions are then discretized in terms of standard 1-D linear finite-elements, on a computational interval that covers the anticipated region of interaction. The field in the fiber is represented by a suitable selection of its vectorial guided modes, superimposed with a-priori unknown amplitudes. One arrives at an approximate expression for the total field as a sum of "modal elements" (elements times slab mode profiles, or fiber mode profiles). Then a projection procedure of Galerkin-type, based on the source-free Maxwell equations in the frequency-domain, leads to a moderately-sized linear system of equations for the unknown coefficients in the template. That system is finally solved by numerical means.

For all further implementational details and adjustments as required for the present 2.5-D setting, we refer to [13, 32]. By construction, the HCMT simulations give direct access to the amplitudes of the fiber modes of interest. Solutions for individual angles of incidence are computationally reasonably cheap, and as such well suited for the simulations of incoming wave bundles, as discussed in Section 4. While the HCMT models are inherently approximative, excellent agreement with rigorous numerical finite-element simulations [33] has been observed [13].

The parameters for the simulations in this paper resemble standard values for silicon thin-film slab waveguides on a silica substrate in air. We consider the configuration of Fig. 1, with a coated dielectric rod of outer-rim radius $\rho = 2\,\mu$m, with refractive indices $n_\mathrm{s} = n_\mathrm{r} = 1.45$ (substrate, fiber core), $n_\mathrm{f} = n_\mathrm{a} = 3.45$ (guiding film, rod coating), and $n_\mathrm{c} = 1.0$ (cladding), for excitation around a target vacuum wavelength $\lambda = 1.55\,\mu$m. The rod coating and the slab waveguide core are of a thickness of $d = a = 0.22\,\mu$m.

The non-symmetric slab waveguide supports fundamental modes of both polarizations with effective indices $N_\mathrm{TE} = 2.8051$ (TE) and $N_\mathrm{TM} = 1.8748$ (TM) [34, 35]. As discussed at the end of Section 2, critical angles θ_c, θ_s, and θ_TM can be defined on the basis of these values. For TE-polarized excitation, radiative losses to the cladding and substrate regions are suppressed for angles of incidence $\theta > \theta_\mathrm{c} = 20.88°$ and $\theta > \theta_\mathrm{s} = 31.13°$, respectively, while scattering to guided TM modes is forbidden for $\theta > \theta_\mathrm{TM} = 41.94°$. In case of incoming TM waves, the critical angles for radiation into the cladding and substrate regions are $\theta_\mathrm{c} = 32.24°$ and $\theta_\mathrm{s} = 50.66°$.

The coated fiber of Fig. 1 is most conveniently described in terms of cylindrical coordinates r, φ, y with the polar origin at the fiber axis. Standard analysis procedures for cylindrical multi-step-index optical fibers [36–39] apply. Our emphasis is on waves with a definite rotational sense, hence we consider the guided modes in the form

$$\begin{pmatrix} \boldsymbol{E} \\ \boldsymbol{H} \end{pmatrix}(r, \varphi, y) = \Big(\boldsymbol{\Psi}(r)\ \mathrm{e}^{-\mathrm{i}l\varphi}\Big)\ \mathrm{e}^{-\mathrm{i}\beta y}. \tag{4}$$

In general these are hybrid vectorial electromagnetic fields $(\boldsymbol{E}, \boldsymbol{H})$ that propagate in axial direction y with real propagation constant $\beta = kN_\mathrm{m}$, where N_m is the effective index of the fiber mode. The mode profile separates into a radial shape $\boldsymbol{\Psi}$ and an angular exponential with integer order l. Following Refs. [40–42], these waves will be called orbital-angular-momentum (OAM)-modes. For the purposes of the present paper, we occasionally use the term "vorticity" for the topological charge, the angular mode order l, of these "vortex"-fields (thus avoiding the task of a precise definition in terms of general electromagnetic quantities [43]).

OAM modes of nonzero angular order are of most interest for our purposes. These come as pairs of exactly degenerate eigen-fields with opposite angular orders l and $-l$. Their vectorial radial shapes differ with respect to signs in specific components. For progressing time, the physical waves in any cross-sectional plane (viewing direction $-y$, cf. Fig. 1(b)) rotate clockwise ($l \geq 1$) or anticlockwise ($l \leq -1$). Note that the well-known modal solutions of HE- or EH-type [44] can be assembled as specific superpositions of degenerate directional OAM modes (these are not of interest for the present paper, however). For zero angular order, one distinguishes two classes of rotationally constant modes. TE modes are characterized by a purely transverse electric field, with zero axial electric component. Likewise, the radial profiles of TM modes have a purely transverse magnetic field and zero axial magnetic component. Hence, in the present context, the fiber modes can be designated by a mode type identifier TE, TM, or OAM, with the angular order l as a first index. A second index m counts modes with that angular order, sorted by effective index, starting at 1 for the mode with highest N_{m}. m can be thought of as being related to a radial order, i.e. modes with growing index show a (not strictly) increasing number of zeros in the radial shapes of their mode profile components. Orthogonal states are distinguished by angular order, radial order, and also polarization, where the two latter are covered by the index m.

The coated air-clad circular fiber constitutes a highly multimode waveguide with (when compared to standard telecom fibers) "giant" refractive index contrast. At the target wavelength, our solver [34, 45] identifies in total 96 orthogonal guided modes. The list covers the azimuthally constant TE(0, 1–3) and TM(0, 1–3)-modes, modes OAM($\pm l$, 1), for $l = 1, 2, \ldots, 20$, and OAM($\pm l$, 2), for $l = 1, 2, \ldots, 11$, of fundamental and first radial order, and further modes OAM($\pm l$, 3), for $l = 1, 2, \ldots, 5$, OAM($\pm l$, 4), for $l = 1, 2, 3$, OAM($\pm l$, 5), for $l = 1, 2$, and OAM(± 1, 6) of higher radial orders. While all OAM modes are strictly hybrid with six nonzero electromagnetic components, the OAM(l, 1) modes (second index 1) show strong axial & azimuthal and weaker radial electric components. If one imagines the curvature of the fiber coating to be decreasing, this relates the OAM(l, 1) fields to the oblique TE modes of the emerging slab waveguide [39]. Likewise, with strong radial but weaker axial & azimuthal electric field components, the OAM(l, 2) modes correspond to the oblique TM modes of the respective slab.

We now return to the full composite structure of Fig. 1. If the fiber is placed in proximity of the half-infinite substrate that supports the guiding film, only modes with effective indices above the level n_{s} can be excited without suffering from losses due to radiation into the substrate region. Of the former list, the rotationally constant modes TE(0, 1) and TM(0, 1), the TE-like modes OAM($\pm l$, 1), for $l = 1, 2, \ldots, 18$, and TM-like modes OAM($\pm l$, 2), for $l = 1, 2, \ldots, 8$ have effective indices N_{m} above n_{s}. Accordingly, we focus on those fewer modes, and we restrict the following simulations to angles of incidence $\theta > \theta_{\mathrm{s}}$ above the critical angle for losses into the substrate.

The incident wave in the slab waveguide can be expected to interact noticeably with a particular mode of the fiber, if the fields are reasonably phase matched. Separately for each mode of the fiber, one defines a critical angle θ_{m} through the relation

$$kN_{\mathrm{in}} \sin\theta_{\mathrm{m}} = kN_{\mathrm{m}} \quad \text{or} \quad \sin\theta_{\mathrm{m}} = N_{\mathrm{m}}/N_{\mathrm{in}}, \tag{5}$$

such that the y-wavenumber associated with the incoming wave coincides with the propagation constant kN_{m} of the mode in the fiber. Resonant features can be anticipated, if the angle of incidence θ is close to one of the values θ_{m} for any of the fiber modes. Further, the distance between fiber and slab will play a role for the strength of the interaction [21, 24]. We therefore choose the angle of incidence θ as our primary variable, with the gap g as a secondary parameter. Figs. 2 – 6 summarize our simulations of the slab-coupled fiber, for the 2.5-D setting with incoming semi-guided plane waves.

The HCMT-template [13] for these simulations, the (approximate) ansatz for the total optical electromagnetic field, covers the directional slab modes of both polarizations, with amplitude functions that are discretized on an interval $z \in \{-4, 4\}\,\mu$m with a regular mesh of stepsize $0.05\,\mu$m. Further, the template includes fiber modes with characteristic angles in an interval $\theta_{\mathrm{m}} \in [\theta - 10°, \theta + 10°]$ around the angle of incidence θ. The HCMT simulations are power conservative; within the limits of numerical accuracy, reflectances R_{TE}, R_{TM} and transmittances T_{TE}, T_{TM} for the fundamental TE and TM slab modes add up to unity.

3.1 Spectra

Figs. 2 and 3 show angular power transmission spectra, for a fiber-slab distance $g = 0.3\,\mu$m, together with amplitudes assigned to specific fiber modes, for either TE- or TM-polarized excitation. Characteristic mode angles $\theta_{\rm m}$ (not all are labelled), and critical angles $\theta_{\rm s}$ for radiative losses and $\theta_{\rm TM}$ for power transfer to TM modes are indicated. Note that, according to Eqs. (5), (3), these angles depend on the effective index $N_{\rm in}$ of the incident field, i.e. differ for TE- and TM-excitation.

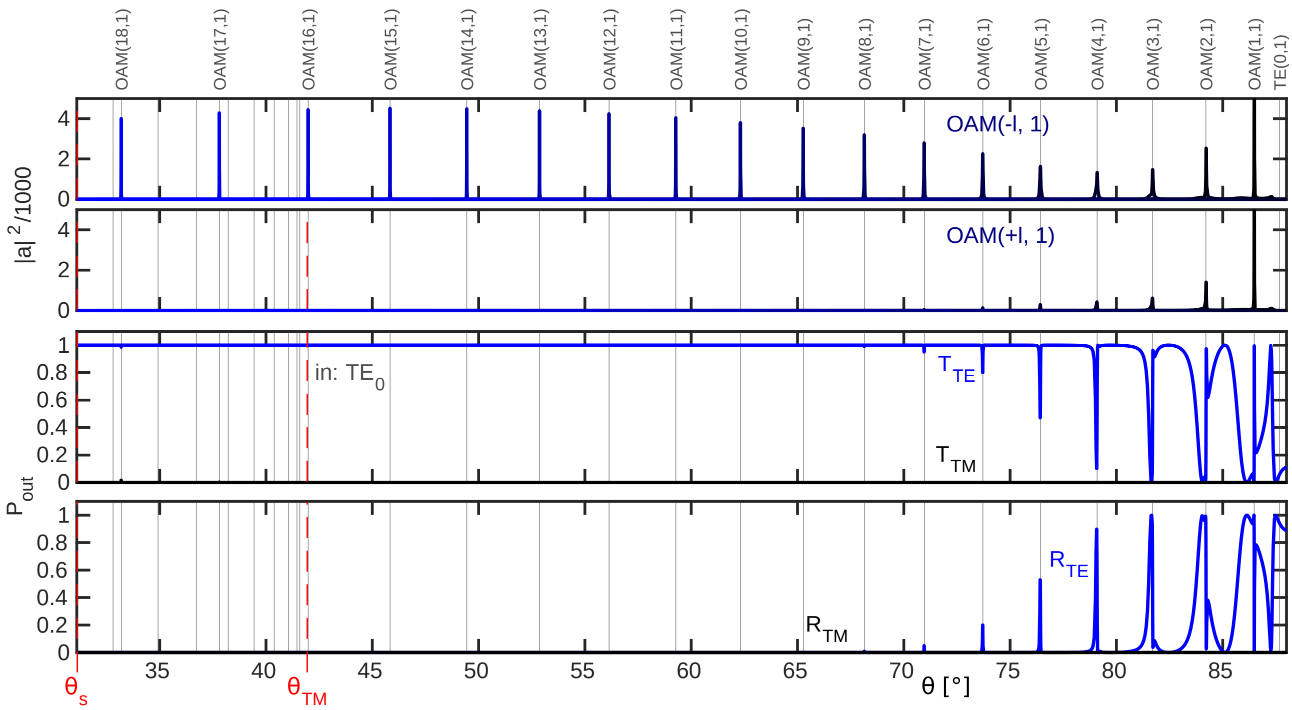

Figure 2: Fiber mode excitation strength and power transmission versus the angle of incidence θ, for a gap distance $g = 0.3\,\mu$m, and excitation by the fundamental TE slab mode. Bottom panels: transmittance T and reflectance R of the TE-and TM-polarized slab modes. Upper plots: amplitudes a of specific fiber modes in the HCMT solution. Curves for OAM modes with mode index $m = 1$ and angular propagation direction (sign of l), of varying angular order $|l|$ share the same axes; the curves largely overlap close to the zero-level. Thin vertical lines: mode angles (5) assigned to individual fiber modes (modes OAM(l, m) and OAM($-l, m$) are strictly degenerate). Curves belonging to OAM modes with different angular order can be identified (with exceptions) by peaks in the vicinity of the respective mode angle.

General trends are as observed in Ref. [13]. The present configuration, with a fiber coating matched to the thin film slab, enables some non-negligible, more or less strong interaction of the incoming slab mode with most of the guided modes of the fiber. Resonances show up as peaks in the amplitude curves of certain fiber modes, accompanied by drops in the transmittances and corresponding peaks in reflectances (in some cases not visible on the scale of the figures).

For the pairs of degenerate modes OAM($\pm l, m$), the precise excitation conditions determine the relative weight of OAM($-l, m$) versus OAM(l, m). We look specifically at the modes with low index $m = 1, 2$, i.e. the modes with fundamental radial order, with fields concentrated in the fiber coating. Modes of lower angular order, with higher effective indices and larger critical angles, experience a more balanced excitation of OAM($-l, m$) and OAM(l, m), with amplitudes of comparable (order of) magnitude. In turn, the field in the fiber then radiates back into the slab in both directions, leading to more pronounced dips/peaks in the transmittance and reflectance curves. The most prominent features appear towards grazing incidence (the curves stop at $\theta = 88°$). This becomes plausible, if one imagines moving along with a wave front of the incoming slab mode: Slab and fiber are closer over a longer propagation distance for increasing excitation angle θ, causing a stronger interaction between the waves.

For growing angular order, however, at resonance the incoming wave is able to transfer its directionality to the field in the fiber. This concerns fiber modes with lower effective index, i.e. lower angles of incidence. Here the simulations predict a strong excitation of the mode OAM($-l, m$) and a substantially lower amplitude of the corresponding OAM(l, m)-mode. The resulting field in the fiber consists almost exclusively of a single OAM mode of high vorticity, with well defined optical angular momentum. That field radiates back into the

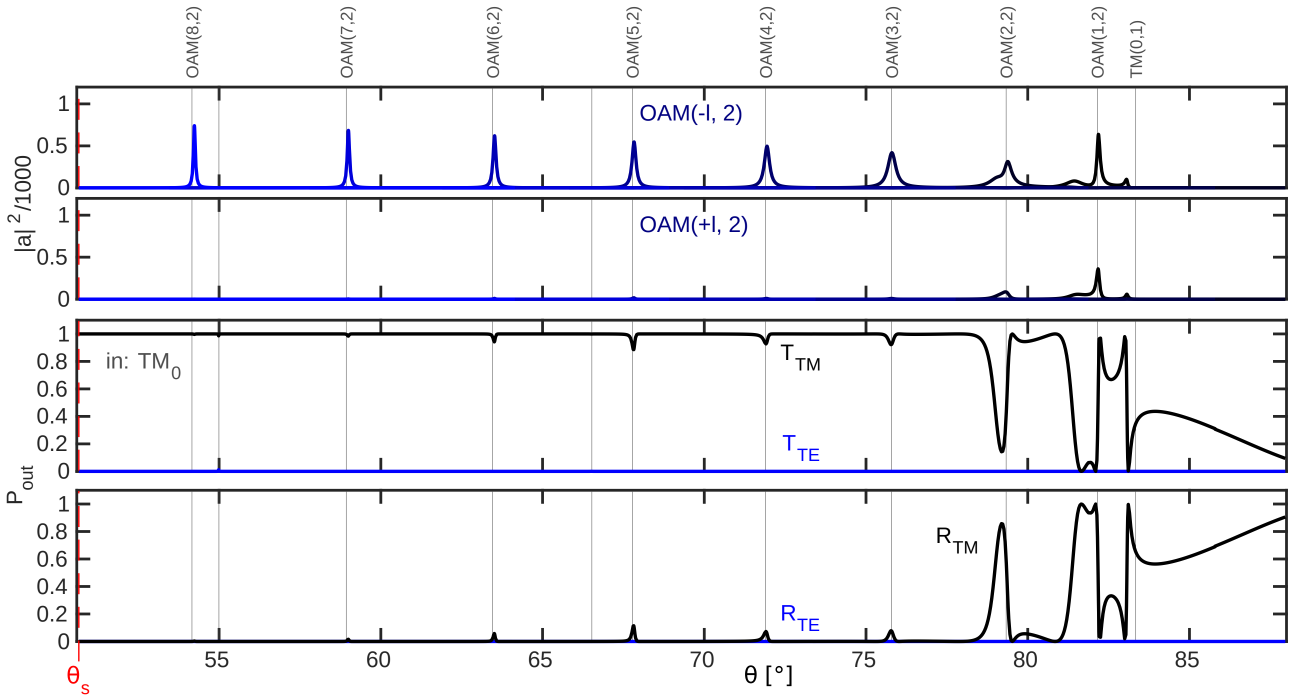

Figure 3: Fiber mode excitation strength and power transmission versus the angle of incidence θ, for a gap distance $g = 0.3\,\mu$m, and excitation by the fundamental TM slab mode. Bottom panels: transmittance T and reflectance R of the TE-and TM-polarized slab modes. Upper plots: amplitudes a of specific fiber modes in the HCMT solution. Curves for OAM modes with mode index $m = 2$ and angular propagation direction (sign of l), of varying angular order $|l|$ share the same axes; the curves largely overlap close to the zero-level. Thin vertical lines: mode angles (5) assigned to individual fiber modes (modes OAM(l, m) and OAM($-l$, m) are strictly degenerate). Curves belonging to OAM modes with different angular order can be identified (with exceptions) by peaks in the vicinity of the respective mode angle.

slab chiefly in the forward $+z$-direction, hence these resonances do not (hardly) show in the transmittance / reflectance curves.

Features are qualitatively alike for both input polarizations. For TE input and the present range of incidence angles, there is only very minor excitation of the TM-like OAM($\pm l$, 2)-modes (amplitudes not shown), and hardly any polarization conversion. The TM fields of both the slab and the fiber are less well confined to their respective cores, with larger field overlaps and wider, less pronounced resonances than for TE input. Note that only fiber modes with effective indices $N_\mathrm{m} < N_\mathrm{TM}$ become accessible (cf. Eq. (5)) by TM excitation.

3.2 Resonances

Next we consider Fig. 4 for a more quantitative inspection of some of the resonances. The figure shows mode amplitude levels $|a|^2$ in an angular range around the critical angle for a specific pair of degenerate fiber modes, comparing curves for varying gaps g. According to Fig. 5, the features translate qualitatively to wavelength or frequency spectra [21, 24]. Here each panel considers either TE- or TM-polarized excitation at an angle of incidence equal to the critical angle (3), at the target wavelength of $\lambda_0 = 1.55\,\mu$m, of the mode in question, such that resonances appear close to λ_0.

As a general trend, for larger distance g, the fiber modes contribute with *growing* amplitudes to the overall fields at resonance. The resonance peaks narrow, become better defined, and appear closer to the critical angle of the fiber mode in question, or closer to the target wavelength, respectively. Roughly equidistant maximum levels on the logarithmic vertical axes indicate an exponential growth of mode amplitudes with the gap distance. This concerns fiber modes that are normalized to unit axial power, and an input, through the slab mode, of unit power per length unit in the y-direction. The large fiber mode amplitudes can thus be translated to respective ratios in field strength, when comparing field levels in the fiber coating and the slab core. In line with the mechanisms discussed in Ref. [24], the simulations predict a field enhancement (and Q-factors, not further explicated here), that grow exponentially with the distance between film and fiber, for the present y-infinite configuration.

A comparison of amplitudes for modes OAM($-l, m$) and OAM(l, m) serves for a quantification of the rota-

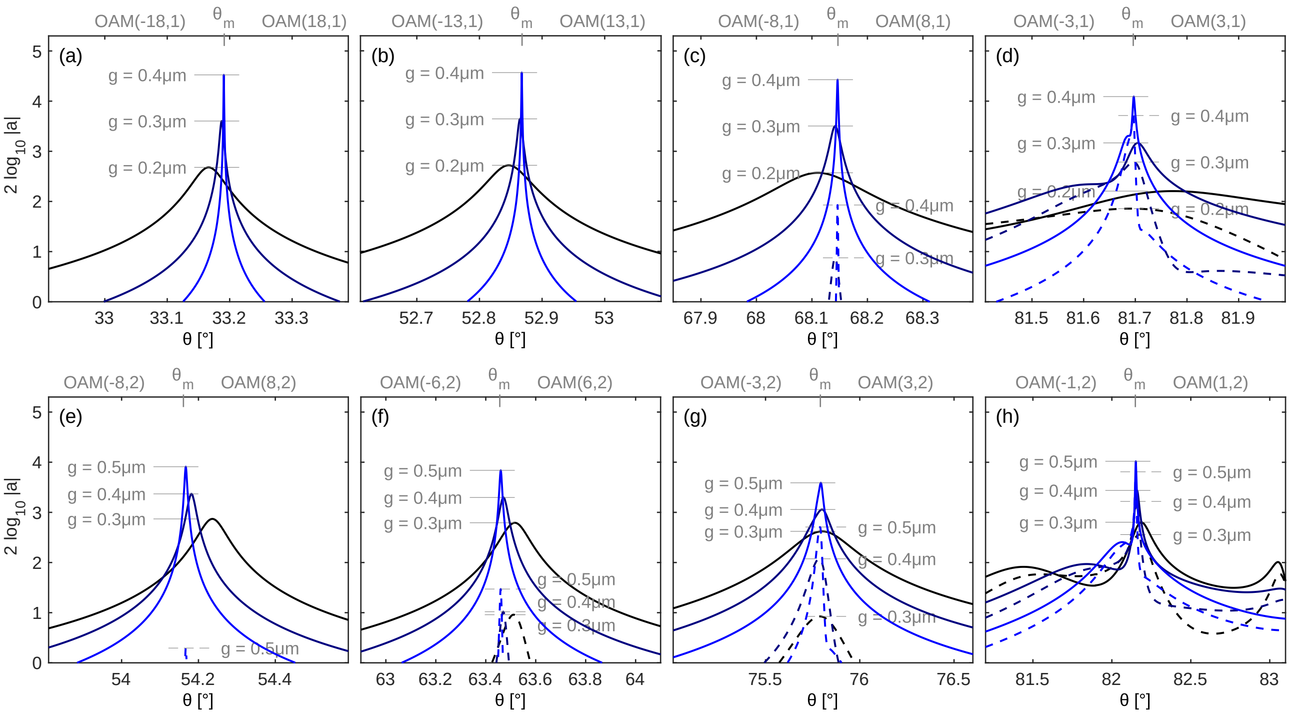

Figure 4: Fiber mode amplitudes $|a|^2$ (logarithmic scale) versus angle of incidence θ, at the target wavelength $\lambda = 1.55\,\mu$m, for different gap values g; excitation by the fundamental TE-mode (a–d) and the fundamental TM-mode (e-h) of the slab. Each panel focuses on one doubly-degenerate fiber mode; curves can be assigned to the mode labels at the top of the panels by the maximum levels (shorter horizontal lines) for specific gaps. Continuous lines correspond to the mode label on the left; dashed lines relate to the mode label on the right, if present.

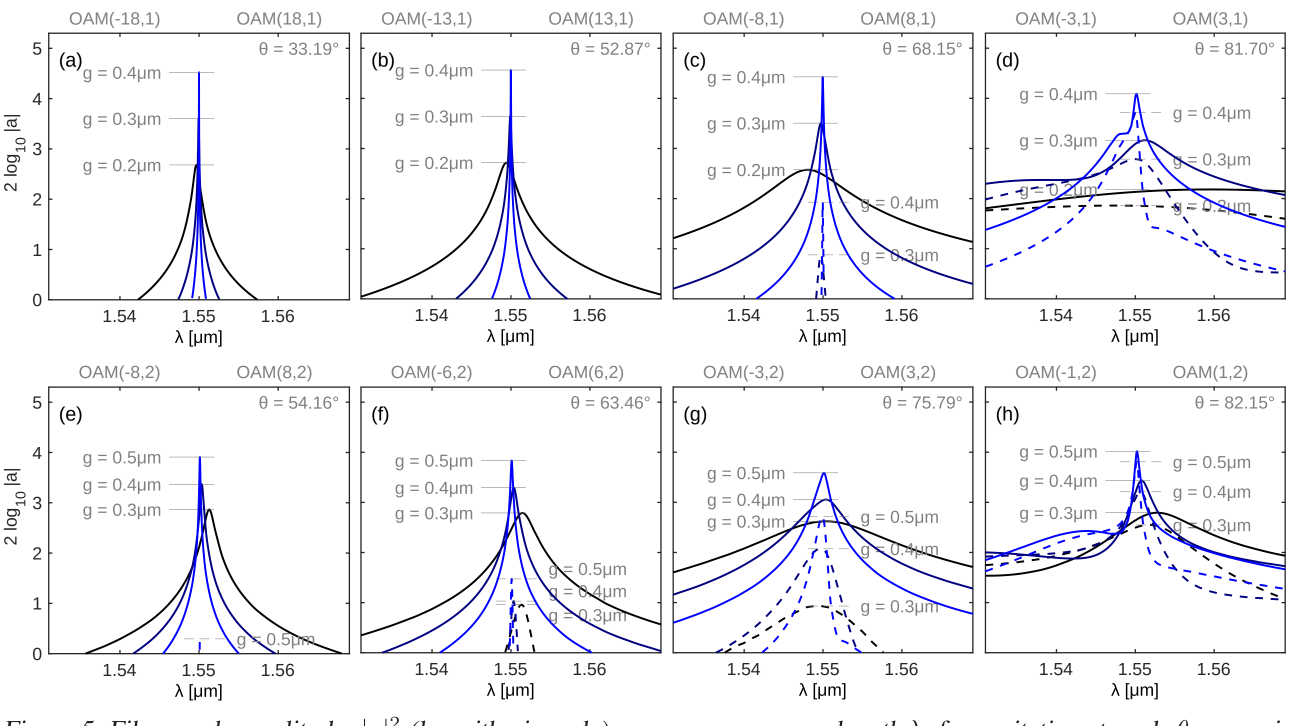

Figure 5: Fiber mode amplitudes $|a|^2$ (logarithmic scale) versus vacuum wavelength λ, for excitation at angle θ as specified, for different gap values g; excitation by the fundamental TE-mode (a–d) and the fundamental TM-mode (e-h) of the slab. Each panel focuses on one doubly-degenerate fiber mode; curves can be assigned to the mode labels at the top of the panels by the maximum levels (shorter horizontal lines) for specific gaps. Continuous lines correspond to the mode label on the left; dashed lines relate to the mode label on the right, if present.

tional directivity of the fields in the fiber at resonance (curves not shown are below the level $|a|^2 = 1$). If both modes are excited with reasonable strength (d, h), the ratio of amplitudes appears roughly independent of g. In particular for the most interesting cases of high-vorticity-modes (a, b, e, f), however, the amplitudes differ by several orders of magnitude. As an example, for the TE-like OAM mode of angular order 13 (which we select for further simulations in Section 4), the levels $|a|^2$ for OAM$(-13, 1)$ and OAM$(13, 1)$ in Fig. 4(b) are related by factors of $3 \cdot 10^8$ ($g = 0.2\,\mu$m), $2 \cdot 10^8$ ($g = 0.3\,\mu$m), and $7 \cdot 10^7$ ($g = 0.4\,\mu$m). Hence, one can conclude that here the oblique excitation mechanism leads to guided fields with excellent angular directivity.

The "purity" of an electromagnetic OAM-field has been defined as the ratio of the power that is carried by a target mode with specific vorticity over the power in the full field [46]. In our case of a superposition of normalized OAM modes, the purity of the field in the region of the fiber can thus be evaluated easily in terms of the mode amplitudes. Again for the example of a resonant excitation of OAM$(-13, 1)$ in Fig. 4(b), we obtain purity levels of $1 - 1 \cdot 10^{-4} = 0.9999$ ($g = 0.2\,\mu$m), $1 - 3 \cdot 10^{-6}$ ($g = 0.3\,\mu$m), and $1 - 2 \cdot 10^{-7}$ ($g = 0.4\,\mu$m). The deviations from a pure field with vorticity $(-)13$ are caused mainly by tiny contributions from neighboring OAM modes with the same rotational sense as the target mode OAM$(-13, 1)$.

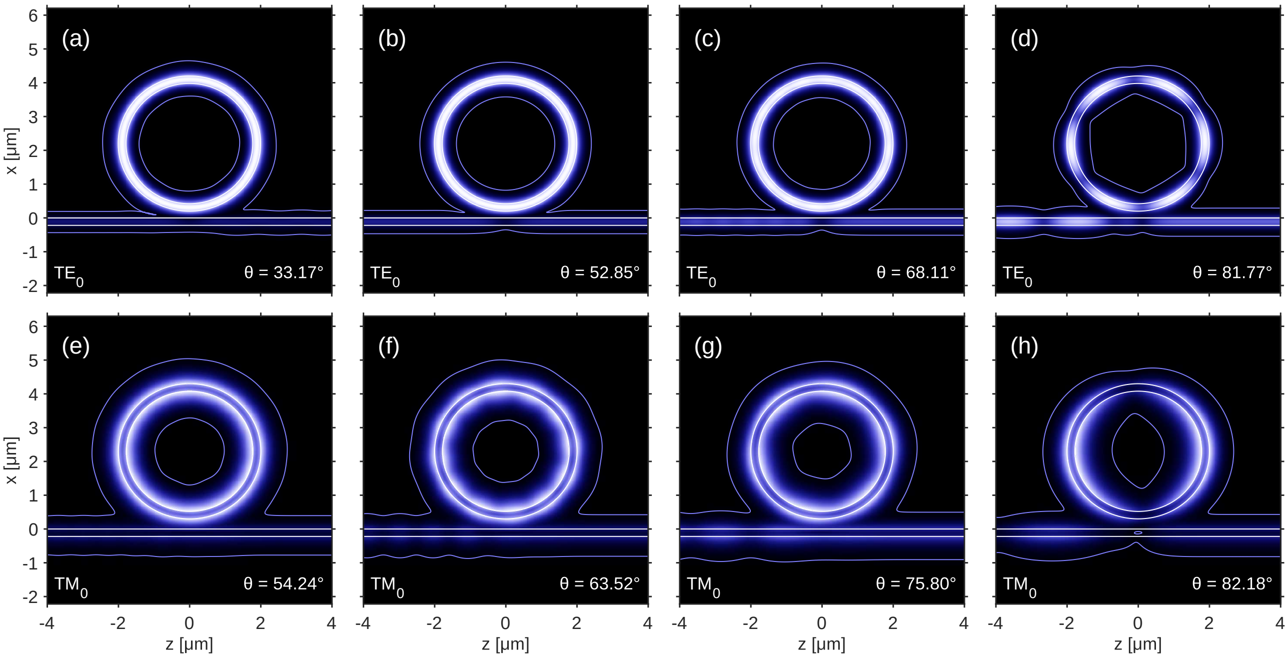

Figure 6: Cross sectional fields $|\boldsymbol{E}|$ (modulus of the vectorial electric field) for excitation of the tube at angles θ that correspond to the maximum levels in Fig. 4, for gaps $g = 0.2\,\mu m$ (TE excitation, panels (a)–(d)) and $g = 0.3\,\mu m$ (TM excitation, panels (e)–(h)). Color scales are adapted to the separate panels, with a contour at 1% of the field maxima.

We complement this section with a look at the resonant field shapes. The panels (a – h) of Fig. 6 correspond to the parameters of Fig. 4(a–h) for polarized incidence at the angle that leads to the maximum amplitude of the OAM$(-|l|, m)$-mode for $g = 0.2\,\mu$m (a–d) and $g = 0.3\,\mu$m (e–h). Up to small shifts in incidence angle, these are also the configurations of Fig. 5(a–h).

In the region of the fiber, one observes the annular shapes of the OAM-mode of fundamental and first radial order, with their field strength confined to the high-index coating. Panels in each row correspond to states with increasingly balanced contributions from two degenerate OAM-modes. From (a) to (d) and from (e) to (h), the interference between modes with negative and positive angular order becomes visible as a rotational modulation of field strength, with nodal lines at $2|l|$ angular positions (more or less discernible in panels (d, f–h) only).

Any field modulation along z in the horizontal film region is caused by interference between forward and backward propagating slab modes, or co-propagation of modes with different polarization. For the states from left to right in each row, along the with more and more comparable amplitudes of the dominant OAM$(\pm l, m)$-modes, the growing reflectance shows an increasingly stronger modulation in the input half $z < 0$ of the slab. A small modulation is also visible in the output half $z > 0$ of the slab in panel (a), where at resonance about 2% of the TE input power is converted to a transmitted TM wave (only just discernible in Fig. 2). Note, however, that the fields in the slab as well as in the fiber are composed of partly co-propagating waves that share a strong y-wavenumber. For destructive interference, field minima appear less prominent as one would expect for strictly counter-propagating waves.

Fig. 6(d) shows a state with predominant resonant excitation of the OAM$(-3, 1)$ mode, transmittance of 66%, reflectance of 34%, for a distance $g = 0.2\,\mu$m. If one looks up that feature in Fig. 2 (but note that those curves are for $g = 0.3\,\mu$m), around $\theta \approx \theta_{\rm m}$ for mode OAM$(\pm 3, 1)$ one notices a prominent peak/dip in the transmittance/reflectance curves, indicating a state with roughly zero transmittance, with a small shoulder at slightly larger θ. Merely that smaller feature actually corresponds to the state with maximum contribution from OAM$(-3, 1)$. Both states can also be identified in Fig. 4(d), by the crossing of the curves for OAM$(-3, 1)$ and OAM$(3, 1)$ (full reflectance) and by the maximum in the curve for OAM$(-3, 1)$, for either g.

4 Wave bundles

All preceding results concern 2.5-D configurations with fields of infinite extent along the fiber axis. Realistic 3-D fields can be constructed by superimposing the former solutions for a range of angles of incidence, or wavenumbers k_y, respectively, such that the incoming wave is of limited width. In line with [16, 18], we choose weights for semi-guided wave bundles of laterally Gaussian shape. The total electromagnetic field then takes the form

$$\begin{pmatrix} \boldsymbol{E} \\ \boldsymbol{H} \end{pmatrix}(x, y, z) = A \int \mathrm{e}^{-\frac{(k_y - k_{y0})^2}{w_k^2}} \left\{ \boldsymbol{\Psi}_{\text{in}}(k_y; x)\, \mathrm{e}^{-\mathrm{i}k_z(k_y)(z - z_0)} + \boldsymbol{\rho}(k_y; x, z) \right\} \mathrm{e}^{-\mathrm{i}k_y(y - y_0)}\, \mathrm{d}k_y. \quad (6)$$

Here the central term in curly brackets represents the HCMT solution, formally separated into a contribution of the incoming field with mode profile $\boldsymbol{\Psi}_{\text{in}}$, and a remainder $\boldsymbol{\rho}$. These solutions for wavenumber k_y are superimposed with a Gaussian weighting of half width w_k, centered around a primary wavenumber $k_{y0} = kN_{\text{in}} \sin\theta_0$, for primary angle of incidence θ_0, with a global amplitude A. Coordinate offsets place the beam focus in the y-z-plane at (y_0, z_0).

The power carried by the incident wave is determined by integrating the z-component of the Poynting vector associated with the input-part (omitting ρ) of the electromagnetic field (6) over the x-y-plane, at some convenient z-position (e.g. at $z = z_0$). Assuming a normalization of $\boldsymbol{\Psi}_{\text{in}}$ to unit power per length unit l in direction y [27], the input beam is normalized to unit input power, if $A = (w_k\sqrt{2\pi^3})^{(-1/2)}\sqrt{l}$.

The incident part of the wave bundle Eq. (6) can be given a little more intuitive form. By assuming a small spectral width w_k, neglecting the effect of the rotation of the vectorial mode profile ($\boldsymbol{\Psi}_{\text{in}}(k_y; x) \approx \boldsymbol{\Psi}_{\text{in}}(k_{y0}; x)$), and introducing the cross section position y' and longitudinal position z', relative to the focus, as new coordinates $y = y_0 + z' \sin\theta_0 + y' \cos\theta_0$, $z = z_0 + z' \cos\theta_0 - y' \sin\theta_0$, one can write the incoming field as

$$\begin{pmatrix} \boldsymbol{E} \\ \boldsymbol{H} \end{pmatrix}_{\text{in}} (x, y', z') \approx \frac{\sqrt{\pi}}{2} A\, w_k\ \mathrm{e}^{-\frac{(y')^2}{(W/2)^2}}\ \boldsymbol{\Psi}_{\text{in}}(k_{y0}; x)\ \mathrm{e}^{-\mathrm{i}kN_{\text{in}}z'}. \quad (7)$$

This is a Gaussian beam in the y-z-plane propagating at angle θ_0. Its width W, the full width of the field at $1/\mathrm{e}$-level, at focus, in the direction y' perpendicular to the beam axis z', is related to the spectral width w_k by $W = (4/w_k)\cos\theta_0$. We use this cross-section-width W, together with the primary angle of incidence θ_0 and the vacuum wavelength λ, to specify the incident field for the examples in this section. Note that none of the additional approximations that lead to the expression (7) enter these simulations.

For the sake of brevity, we limit the following discussion to incoming TE waves, i.e. to the the excitation of OAM$(-l, 1)$ modes only. Quantitatively similar results are to be expected for the OAM$(-l, 2)$-excitation by TM polarized slab modes. Even more specifically, and rather arbitrarily, we focus on one particular high-vorticity mode OAM$(-13, 1)$ with effective mode index $N_{\text{m}} = 2.2364$ and critical angle $\theta_{\text{m}} = 52.8680°$: According to Fig. 2, its resonance is located conveniently between angular regions where polarization conversion might complicate matters, or where the rotational directionality of the resonant fields is lower.

This then concerns simulations for a range of angles of incidence, where the individual fiber modes contribute to the overall solution in narrow and well separated angular intervals. Hence, for reasons of reducing the computational effort, we restrict the HCMT template to mode angles in an interval of 10°-width centered at the respective angle of incidence. For our target mode OAM$(-13, 1)$, according to Fig. 2, this implies that merely the fiber modes OAM$(\pm 12, 1)$, OAM$(\pm 13, 1)$, and OAM$(\pm 14, 1)$ are included. For the evaluation of the field of the bundle (6), we apply numerical quadrature procedures [47]. Care must be taken to ensure convergence. On the one hand, the resonant response of the slab-coupled fiber (cf. Fig. 4) needs to be resolved properly. On the other hand, relevant values for the beam width W, or the spectral width parameter w_k, respectively, span several orders of magnitude.

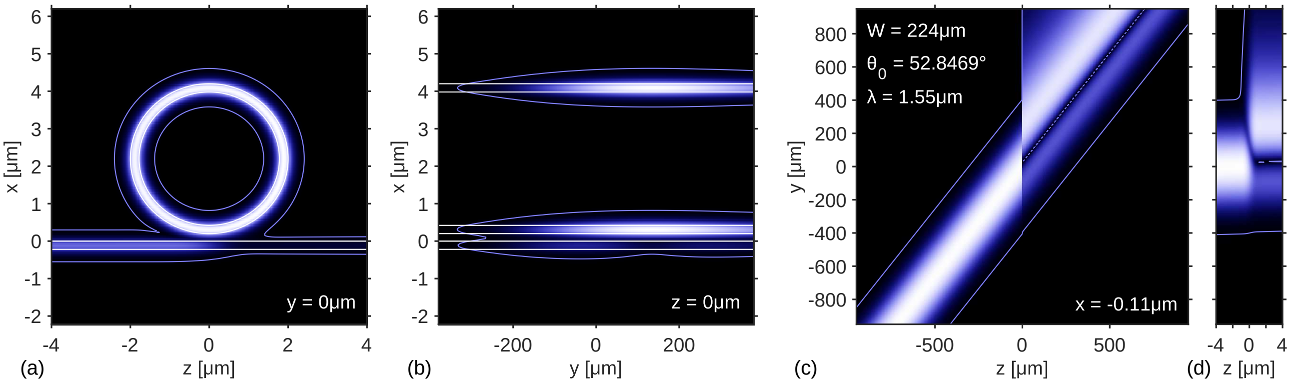

Figure 7: Oblique evanescent excitation of the structure of Fig. 1, for gap $g = 0.2\,\mu$m, by a TE-polarized bundle of cross sectional width W at primary angle of incidence θ_0 and vacuum wavelength λ. The panels show the absolute electric field $|\boldsymbol{E}|$ on the fiber cross section plane at $y = 0\,\mu$m (a), on the vertical plane including the fiber axis at $z = 0\,\mu$m (b), and on the horizontal plane at the slab center $x = -d/2$ (c, d). Color scales are adapted to the field range on the individual plots, with a contour at 1% of the respective maxima.

Fig. 7 gives an impression of a field that is generated by these simulations. As we shall argue below, the parameters define a configuration with, in a certain sense, optimal excitation. Note the axes' gross difference in range.

Panel (a) shows a cross section view at the y-position where the center of the incoming beam traverses the fiber. Just as in Fig. 6(b), one observes a strong field in the fiber without modulation, indicating a wave with full rotational directionality, with no, or only a weak contribution of OAM$(13, 1)$. Likewise, the absence of any modulation in the slab waveguide for $z < 0$ signifies forward wave propagation only, with no, or hardly any reflections. Unlike Fig. 6(b), however, panel Fig. 7(a) shows only a weak field in the slab waveguide for $z > 0$. There is much lower direct transmission, the optical power apparently enters the fiber in the region of strongest interaction at $z = 0$. Accordingly, in the field section (b) along the axis coordinate, one observes a gradual accumulation of power in the fiber, with a maximum reached at a position $y > 0$ a little further than the beam focus at $y = 0$, followed by a slower gradual decay of intensity. This becomes also apparent in the "top/bottom" view (c). A major part of the power in the incoming beam appears to enter the fiber, and then leaks back to the slab waveguide, while propagating along the fiber. In this process, the waves keep to the forward ($+z$-, $+y$-) and anti-clockwise ($-\varphi$-) direction of propagation. Note that, for the ranges of the z-axes as shown, the plots on the y-z-planes in Figs. 7(c) and 11 cannot resolve the field variation across the $4\,\mu$m fiber diameter; the fields appear discontinuous at $z = 0$ (according to Figs. 7(a, d), they are not).

We now return to our original aim, the excitation of a strong field in-fiber, with large vorticity. More specifically, after our preparations, we aim at a large amplitude of the OAM$(-13, 1)$ mode: For an incoming semi-guided Gaussian beam of given input power, a fraction as large as possible of that power should be channelled into the OAM$(-13, 1)$ mode. We thus trace the local mode amplitude as a function of position along the y-axis. The amplitude is computed by projecting [28] the 3-D bundle solution (6) at the respective y-position onto the normalized profile of the OAM$(-13, 1)$-mode. This corresponds to (the square-root of) the relative output power P_f that could be expected in a structure, where the slab is cut away in the x-z-plane at y, and merely the fiber continues (in this reasoning, reflections and radiation losses of the fiber-bound part of the field, due to the slab discontinuity in its evanescent tail, are neglected).

Further, the achievable strength of the vortex field in the fiber might be of interest, relative to the maximum field strength in the input beam. To that end we record the absolute electric field $|\boldsymbol{E}_\mathrm{f}|^2$ on a line along y at the position $x = g + 2\rho - a/2$, $z = 0$ in the cladding center at the "top" of the fiber, and the field strength $|\boldsymbol{E}_\mathrm{in}|^2$ on a cross section of the input beam at the center $x = -d/2$ of the slab core, at a position $y = -W/\cos(\theta_0)$ "before" the beam encounters the fiber. The ratio $A_\mathrm{f} = (\max_y |\boldsymbol{E}_\mathrm{f}|^2)/(\max_z |\boldsymbol{E}_\mathrm{in}|^2)$ then gives an indication of the field amplification slab-to-fiber, at resonance. Figs. 8–10 summarize the results of respective simulations, as before for gap distances $g = 0.2, 0.3, 0.4\,\mu$m.

Aiming at a strong excitation, the original vacuum wavelength, and an angle of incidence close to the critical angle of the target mode, are rather obvious choices. To shed some light on the perhaps less obvious role of the beam width parameter, Fig. 8 shows the power P_f assigned to the OAM$(-13, 1)$-mode, as a function of position y along the fiber axis, for incoming beams of differing width W. Just as in Fig. 9, the primary angle of

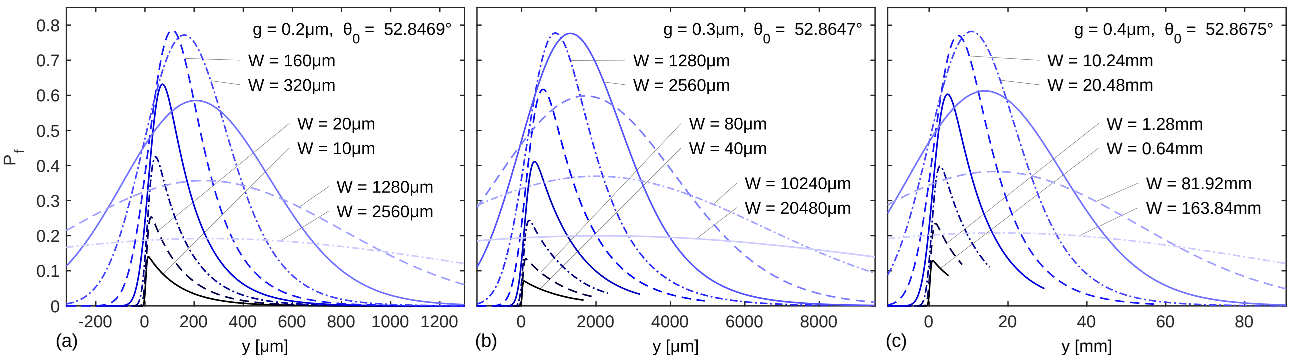

Figure 8: Relative power P_f attributed to the OAM$(-13, 1)$-mode at positions y along the fiber axis, for varying cross-sectional width W of the incident semi-guided wave bundle, increasing from a minimum W (darkest curve) to a largest value (light) by factors of 2. Panels (a)-(c) correspond to gap distances $g = 0.2, 0.3, 0.4\,\mu$m, with bundles at slightly differing primary angles of incidence θ_0.

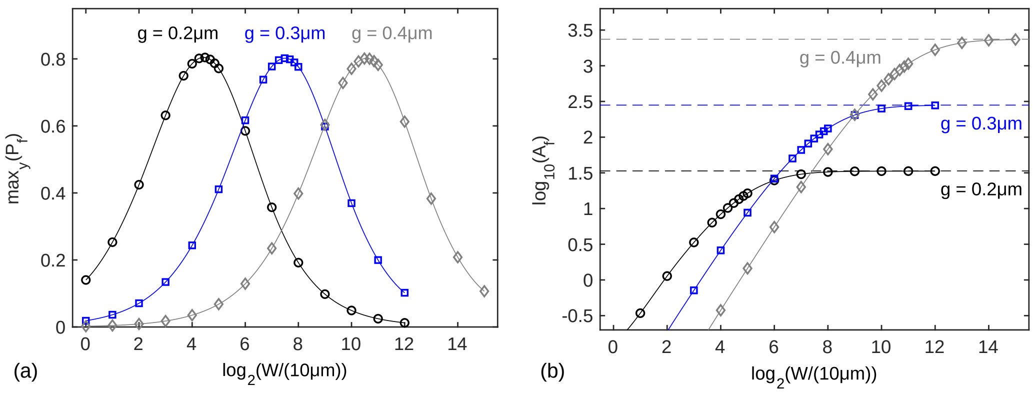

Figure 9: Maxima $\max_y P_f$ of the relative power carried by the OAM$(-13, 1)$-mode at different positions y along the fiber axis (a), and amplification factors A_f for the squared electric field in the fiber (b), versus the cross-sectional width W of the bundle. Curves for combinations of gap and primary angle of incidence $g = 0.2\,\mu$m, $\theta_0 = 52.8469°$ (circles), $g = 0.3\,\mu$m, $\theta_0 = 52.8647°$ (squares), $g = 0.4\,\mu$m, $\theta_0 = 52.86754°$ (diamond markers) are shown. The dashed lines in part (b) indicate limiting levels of field ratios 34 ($g = 0.2\,\mu$m), 281 ($g = 0.3\,\mu$m), 2351 ($g = 0.4\,\mu$m), for an incoming semi-guided plane wave of unlimited lateral extension.

incidence has been adjusted, for each g, to the values at which $|a|^2(\theta)$ is at maximum in Fig. 4(b). With a rapid increase of P_f with y, followed by a more gradual decrease, in Fig. 8 one observes a behaviour in qualitative accordance with Fig. 7(b,c). The extent, “symmetry”, and maxima of the P_f-vs.y-curves, however, change drastically with the beam width W. For fixed gap g and growing W of the wave bundle, the maximum (vs. y) power transferred to the target mode first grows, reaches a certain maximum, then drops again, where the maximum level appears to be independent of g. This pattern is also highlighted in Fig. 9(a).

The features can be interpreted as follows. In the formation of the maximum power level, two spectral functions (of y-wavenumbers, or angles of incidence) play a role. These are the shape of the excitation amplitude, the resonant response of the fiber-slab-structure, on the one hand, and the spectrally Gaussian shape of the incoming wave bundle (6) on the other hand. Of these, the former depends on the gap distance, as shown in Fig. 4(b). The latter narrows down, with increasing beam width W, from a spectral width that is much wider than the resonance in excitation amplitude to a wavenumber range much smaller than that resonance. According to both Figs. 8 and 9(a), the maximum achievable level P_f of relative power transfer to the OAM$(-13, 1)$ mode is, for the distances considered here, independent from g. For growing g, however, the maximum is reached for incoming bundles of growing widths. This points at a mechanism, where the Gaussian spectral shape of the incoming bundle needs to match the spectral shape of the excitation amplitude in Fig. 4(d) for maximum transferred power. The optimum matching then determines the upper level as observed.

To support this hypothesis, one might consider overlaps of normalized spectral line shapes of Gaussian and Lorentzian type, of independently varying spectral width. Their L^2-inner product reaches a maximum, if the full-width-at-half-maximum (FWHM) of the Gaussian is roughly 1.3 times the FWHM of the Lorentzian, *independent* of the actual width of either function. Likewise, if one compares the FWHM of the Gaussian weight in Eq. (6) for the beam widths W that correspond to the maxima in Fig. 9(a), translated to an angular range, and the FWHM of the excitation amplitudes in Fig. 4(d), one obtains factors of about 1.4 for the three gap distances as considered (where we do not claim that the functions in Fig. 4(d) are of Lorentzian shape).

For input beams of increasing width, once the maximum of P_f has been reached, the subsequent drop in intensity in the fiber can also be attributed to the distribution of the input power over a growing spatial range, i.e. to a lowering maximum amplitude of the input beam. Still, for very wide beams, one can expect states that approximate the former configurations with y-infinite input. Accordingly, in Fig. 9(b) the ratio of maximum field amplitudes A_f reaches the levels at resonance of the 2.5-D simulations, for widening incoming bundles that more and more resemble the incoming plane wave as considered in Section 3.

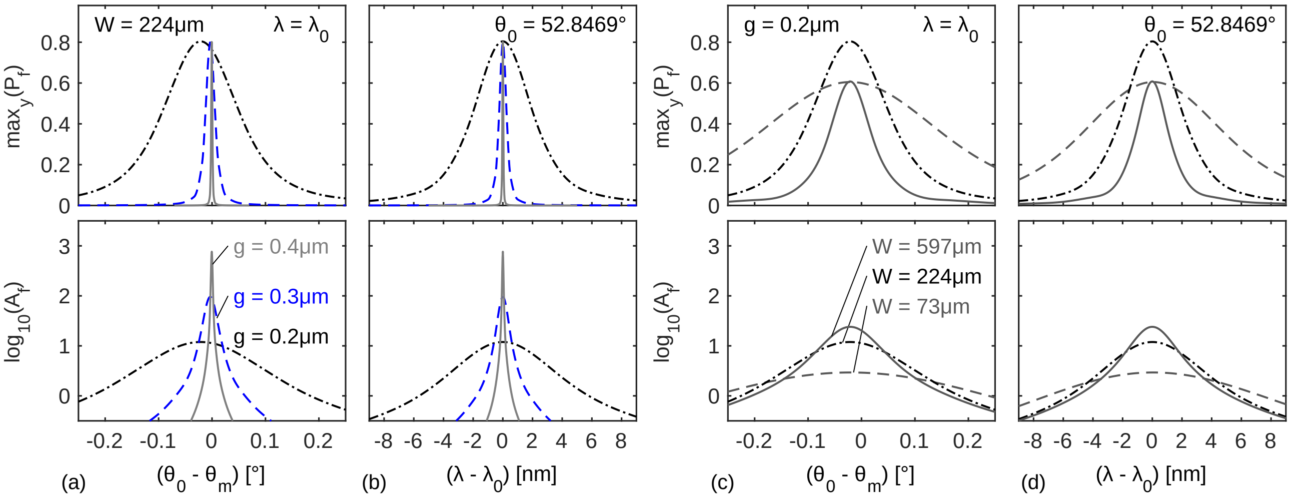

Figure 10: Maximum relative powers $\max_y P_\mathrm{f}$ carried by the OAM$(-13, 1)$-mode, and field amplification factors A_f, versus the primary bundle angle θ_0 (a, c), and as a function of vacuum wavelength λ (b, d); excitation of configurations with different gaps $g = 0.2\,\mu$m (dash-dotted), $g = 0.3\,\mu$m (dashed), $g = 0.4\,\mu$m (continuous lines) by bundles of width $W = 224\,\mu$m (a, b), and for excitation of the structure with gap $g = 0.2\,\mu$m by bundles of different widths $W = 73\,\mu$m (dashed), $W = 224\,\mu$m (dash-dotted), $W = 597\,\mu$m (continuous lines), (c, d). Offsets: target wavelength $\lambda_0 = 1.55\,\mu$m, and critical angle $\theta_m = 52.8680°$ of the OAM$(-13, 1)$-mode.

According to the previous discussion, with a level $\max_y P_\mathrm{f} = 0.804$, the configuration of Fig. 7 is close to optimal what concerns the power in the OAM$(-13, 1)$-mode, but less optimal in field enhancement A_f. In the choice of experimental parameters, however, also sensitivity considerations might play a role. Fig. 10 shows that it can be beneficial to sacrifice a little in P_f or A_f for some gain in tolerance. The configuration of Fig. 7 for $g = 0.2\,\mu$m is less strict in requirements on both angle of incidence (a) and wavelength (b) than the setups for larger gaps with higher field enhancement. Likewise, one might further relax the tolerances in incidence angle (c) and in wavelength (d), if one chooses a narrower input bundle, thereby accepting a moderately lower output P_f to the fiber.

We conclude this section with a look at some configurations with less optimum excitation conditions. Fig. 11 shows field profiles in the horizontal y-z-plane at the elevation of the slab center. Also panel (c) of Fig. 7 can be grouped into this series. Panels (a) and (d) correspond to input beams of smaller (a) and larger width (d); both lead to an output $\max_y P_\mathrm{f} = 0.61$, of about $3/4$ of the maximum level. For the wider input (d), however, large power levels are present in the fiber over a longer range y, when compared to the configuration (a) with the more focused beam. Examples (b, c, e, f) show results for the optimum input beam width, but for off-resonance values of incidence angles (b, e) or vacuum wavelengths (c, f). In these cases, the fiber receives lower fractions of power $\max_y P_\mathrm{f}$ of 0.41 (b), 0.62 (c), 0.08 (e), and 0.04 (f). Positive or negative deviations of the same magnitude, in angle or wavelength, respectively, lead to very similar field pattern (not shown). Off resonance (e, f), the incident semi-guided beam passes by underneath the fiber with hardly any disturbance.

5 Concluding remarks

Modes with high orbital angular momentum supported by a circular step-index optical fiber can interact efficiently with bundles of semi-guided waves in a slab close to the fiber. For the particular examples with wave bundles of laterally Gaussian shape, our simulations predict an upper limit of about 80% for the relative input

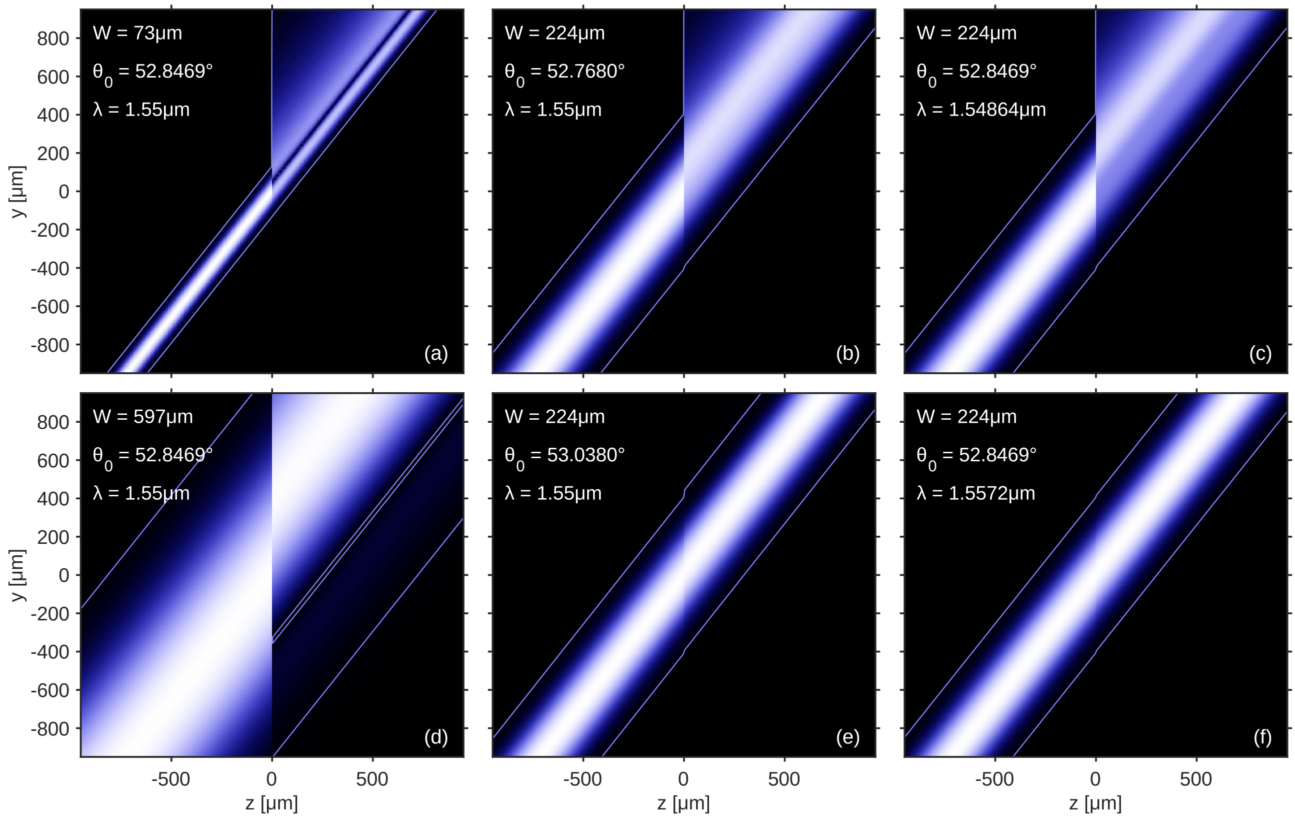

Figure 11: Excitation of the slab coupled coated fiber of Fig. 1, for gap $g = 0.2\,\mu$m, by TE-polarized bundles of cross sectional width W at primary angles of incidence θ_0 and vacuum wavelengths λ. The plots show the absolute electric field $|\boldsymbol{E}|$ on the horizontal plane at the slab center $x = -d/2$. Color scales are adapted to the field range on the individual panels, with a contour at 1% of the respective maxima.

power that can be diverted into an OAM mode with vorticity 13, with a distinction between degenerate modes of opposite angular momentum by several orders of magnitude.

For the present paper, we have considered circular fibers with a high-index coating (index profile $1.45 : 3.45 : 1.0$), excited through a standard silicon-photonics slab ($1.45 : 3.45 : 1.0$), where, over the distance required for the coupling, the fiber is assumed to be suspended in air. Alternatively, one could imagine the fiber embedded in a suitable cladding medium, e.g. a suitable index matching fluid, such that the angle of incidence can still be adjusted. With a cladding of index 1.45 one would then realize a structure with symmetric index profiles as in Ref. [13].

As a further configuration of practical interest one might think of a thin radially homogeneous circular dielectric rod, i.e. an unclad (pulled) multimode fiber (index profile, say, 1.47:1.0). It should also be possible to excite specific OAM modes via the mechanism as discussed in this paper. To ensure reasonable phase matching, excitation could be attempted with a suitably thin Si_3N_4-slab (1.45:2.0:1.0) on an SiO_2-substrate (buffer). Then one would have to deal with a, on the scale of angle of incidence, denser distribution of OAM modes. Some of the interesting modes with higher orbital angular momentum would have effective indices below 1.45, i.e. would leak into the substrate (unless the slab is prepared as a membrane suspended in air).

Our simulations rely on solutions for the axially infinite 2.5-D problems by the hybrid coupled mode technique. In cases where a leakage mechanism might be present that is not covered by the CMT templates, the CMT data can be replaced by rigorous numerical results [13, 24]. Models in terms of laterally confined wave bundles, as described in this paper, should then provide a convenient way for exploring also these alternative configurations.

Funding

Financial support from the German Research Foundation (Deutsche Forschungsgemeinschaft DFG, project 231447078–TRR 142, subproject C05) is gratefully acknowledged.

References

[1] L. Allen, M. W. Beijersbergen, R. J. C. Spreeuw, and J. P. Woerdman. Orbital angular momentum of light and the transformation of laguerre-gaussian laser modes. *Physical Review A*, 45:8185–8189, 1992.

[2] S. Franke-Arnold, L. Allen, and M. Padgett. Advances in optical angular momentum. *Laser & Photonics Reviews*, 2(4):299–313, 2008.

[3] A. M. Yao and M. J. Padgett. Orbital angular momentum: origins, behavior and applications. *Advances in Optics and Photonics*, 3(2):161–204, 2011.

[4] A. E. Willner, H. Huang, Y. Yan, Y. Ren, N. Ahmed, G. Xie, C. Bao, L. Li, Y. Cao, Z. Zhao, J. Wang, M. P. J. Lavery, M. Tur, S. Ramachandran, A. F. Molisch, N. Ashrafi, and S. Ashrafi. Optical communications using orbital angular momentum beams. *Advances in Optics and Photonics*, 7(1):66–106, 2015.

[5] J. Wang. Advances in communications using optical vortices. *Photonics Research*, 4(5):B14–B28, 2016.

[6] S. S. R. Oemrawsingh, J. A..W. van Houwelingen, E. R. Eliel, J. W. Woerdman, E. J. K. Verstegen, J. G. Kloosterboer, and G. W. 't Hooft. Production and characterization of spiral phase plates for optical wavelengths. *Applied Optics*, 43(3):688–694, 2004.

[7] M. W. Beijersbergen, L. Allen, H. E. L. O van der Veen, and J. P. Woerdman. Astigmatic laser mode converters and transfer of orbital angular momentum. *Optics Communications*, 96(1):123–132, 1993.

[8] L. Zhu and J. Wang. Arbitrary manipulation of spatial amplitude and phase using phase-only spatial light modulators. *Scientific Reports*, 4:7441, 2015.

[9] Z. Lin, A. Wang, L. Xu, X. Zhang, B. Sun, C. Gu, and H. Ming. Generation of optical vortices using a helical fiber Bragg grating. *Journal of Lightwave Technology*, 32(11):2152–2156, 2014.

[10] L. Fang and J. Wang. Mode conversion and orbital angular momentum transfer among multiple modes by helical gratings. *IEEE Journal of Quantum Electronics*, 52(8):1–6, 2016.

[11] Y. Yan, J. Wang, L. Zhang, J-Y. Yang, I.-M. Fazal, N. Ahmed, B. Shamee, A.-E. Willner, K. Birnbaum, and S. Dolinar. Fiber coupler for generating orbital angular momentum modes. *Optics Letters*, 36(21):4269–4271, 2011.

[12] J. Fan, J. Zhao, L. Shi, N. Xiao, and M. Hu. Two-channel, dual-beam-mode, wavelength-tunable femtosecond optical parametric oscillator. *Advanced Photonics*, 2(4):1–5, 2020.

[13] M. Hammer, L. Ebers, and J. Förstner. Hybrid coupled mode modelling of the evanescent excitation of a dielectric tube by semi-guided waves at oblique angles. *Optical and Quantum Electronics*, 52:472, 2020.

[14] M. Hammer, L. Ebers, A. Hildebrandt, S. Alhaddad, and J. Förstner. Oblique semi-guided waves: 2-D integrated photonics with negative effective permittivity. In *2018 IEEE 17th International Conference on Mathematical Methods in Electromagnetic Theory (MMET)*, pages 9–15, 2018.

[15] M. Hammer, A. Hildebrandt, and J. Förstner. How planar optical waves can be made to climb dielectric steps. *Optics Letters*, 40(16):3711–3714, 2015.

[16] M. Hammer, A. Hildebrandt, and J. Förstner. Full resonant transmission of semi-guided planar waves through slab waveguide steps at oblique incidence. *Journal of Lightwave Technology*, 34(3):997–1005, 2016.

[17] L. Ebers, M. Hammer, and J. Förstner. Oblique incidence of semi-guided planar waves on slab waveguide steps: Effects of rounded edges. *Optics Express*, 26(14):18621–18632, 2018.

[18] M. Hammer, L. Ebers, and J. Förstner. Oblique quasi-lossless excitation of a thin silicon slab waveguide: a guided-wave variant of an anti-reflection coating. *Journal of the Optical Society of America B*, 36(9):2395–2401, 2019.

[19] E. A. Bezus, L. L. Doskolovich, D. A. Bykov, and V. A. Soifer. Spatial integration and differentiation of optical beams in a slab waveguide by a dielectric ridge supporting high-Q resonances. *Optics Express*, 26(19):25156–25165, 2018.

[20] E. A. Bezus, D. A. Bykov, and L. L. Doskolovich. Bound states in the continuum and high-Q resonances supported by a dielectric ridge on a slab waveguide. *Photonics Research*, 6(11):1084–1093, 2018.

[21] L. Ebers, M. Hammer, M. B. Berkemeier, A. Menzel, and J. Förstner. Coupled microstrip-cavities under oblique incidence of semi-guided waves: a lossless integrated optical add-drop filter. *OSA Continuum*, 2(11):3288–3298, 2019.

[22] D. A. Bykov, E. A. Bezus, and L. L. Doskolovich. Bound states in the continuum and strong phase resonances in integrated gires-tournois interferometer. *Nanophotonics*, 9(1):83–92, 2020.

[23] J. Chen and P. Chu. Phase-induced Fano antiresonance in a planar waveguide with two dielectric ridges. *Journal of the Optical Society of America B*, 36(12):3417–3427, 2019.

[24] M. Hammer, L. Ebers, and J. Förstner. Oblique evanescent excitation of a dielectric strip: A model resonator with an open optical cavity of unlimited Q. *Optics Express*, 27(7):9313–9320, 2019.

[25] M. Hammer. Oblique incidence of semi-guided waves on rectangular slab waveguide discontinuities: A vectorial QUEP solver. *Optics Communications*, 338:447–456, 2015.

[26] W. Biehlig and U. Langbein. Three-dimensional step discontinuities in planar waveguides: Angular-spectrum representation of guided wavefields and generalized matrix-operator formalism. *Optical and Quantum Electronics*, 22(4):319–333, 1990.

[27] M. Lohmeyer and R. Stoffer. Integrated optical cross strip polarizer concept. *Optical and Quantum Electronics*, 33(4/5):413–431, 2001.

[28] C. Vassallo. *Optical Waveguide Concepts*. Elsevier, Amsterdam, 1991.

[29] D. G. Hall and B. J. Thompson, editors. *Selected Papers on Coupled-Mode Theory in Guided-Wave Optics*, volume MS 84 of *SPIE Milestone Series*. SPIE Optical Engineering Press, Bellingham, Washington USA, 1993.

[30] W. P. Huang. Coupled mode theory for optical waveguides: an overview. *Journal of the Optical Society of America A*, 11(3):963–983, 1994.

[31] M. Hammer. Guided wave interaction in photonic integrated circuits — a hybrid analytical / numerical approach to coupled mode theory. In A. Agrawal, T. Benson, R. DeLaRue, and G. Wurtz, editors, *Recent Trends in Computational Photonics*, volume 204 of *Springer Series in Optical Sciences*, chapter 3, pages 77–105. Springer, Cham, 2017.

[32] M. Hammer. Hybrid analytical / numerical coupled-mode modeling of guided wave devices. *Journal of Lightwave Technology*, 25(9):2287–2298, 2007.

[33] Comsol Multiphysics GmbH, Göttingen, Germany; http://www.comsol.com.

[34] M. Hammer. METRIC — Mode expansion tools for 2D rectangular integrated optical circuits. http://metric.computational-photonics.eu/.

[35] M. Hammer. OMS — 1-D mode solver for dielectric multilayer slab waveguides. http://www.computational-photonics.eu/oms.html.

[36] C. Yeh. Guided-wave modes in cylindrical optical fibers. *IEEE Transactions on Education*, E-30(1):43–51, 1987.

[37] A. W. Snyder and J. D. Love. *Optical Waveguide Theory*. Chapman and Hall, London, New York, 1983.

[38] C. Brunet, B. Ung, P. Bélanger, Y. Messaddeq, S. LaRochelle, and L. A. Rusch. Vector mode analysis of ring-core fibers: Design tools for spatial division multiplexing. *Journal of Lightwave Technology*, 32(23):4648–4659, 2014.

[39] L. Ebers, M. Hammer, and J. Förstner. Spiral modes supported by circular dielectric tubes and tube segments. *Optical and Quantum Electronics*, 49(4):176, 2017.

[40] N. Bozinovic, Y. Yue, Y. Ren, M. Tur, P. Kristensen, H. Huang, A. E. Willner, and S. Ramachandran. Terabit-scale orbital angular momentum mode division multiplexing in fibers. *Science*, 340(6140):1545–1548, 2013.

[41] L. Wang, P. Vaity, S. Chatigny, Y. Messaddeq, L. A. Rusch, and S. LaRochelle. Orbital-angular-momentum polarization mode dispersion in optical fibers. *Journal of Lightwave Technology*, 34(8):1661–1671, 2016.

[42] J. D. Johnson, Z. Ma, M. J. Padgett, and S. Ramachandran. Measurement of the spin-orbit coupling interaction in ring-core optical fibers. *OSA Continuum*, 2(10):2975–2982, 2019.

[43] M. V. Berry. Optical currents. *Journal of Optics A: Pure and Applied Optics*, 11:094001, 2009.

[44] A. Kapoor and G. S. Singh. Mode classification in cylindrical dielectric waveguides. *Journal of Lightwave Technology*, 18(6):849–852, 2000.

[45] M. Hammer. FiMS — Modes of circular multi-step index optical fibers. http://www.computational-photonics.eu/fims.html.

[46] C. Sun, J. Zhang, B. Xiong, J. Wang, Z. Hao, L. Wang, Y. Han, H. Li, and Y. Luo. Analysis of OAM mode purity of integrated optical vortex beam emitters. *IEEE Photonics Journal*, 9(1):1–7, 2017.

[47] W. H. Press, S. A. Teukolsky, W. T. Vetterling, and B. P. Flannery. *Numerical Recipes in C, 2nd ed.* Cambridge University Press, 1992.